

A crack-tip element for modelling arbitrary crack propagations

Fu, Qiang; Yi, Sinan; Chen, Boyang; Bui, Tinh Quoc; Hu, Xiaofei; Yao, Weian

DOI

[10.1016/j.tafmec.2019.102422](https://doi.org/10.1016/j.tafmec.2019.102422)

Publication date

2020

Document Version

Final published version

Published in

Theoretical and Applied Fracture Mechanics

Citation (APA)

Fu, Q., Yi, S., Chen, B., Bui, T. Q., Hu, X., & Yao, W. (2020). A crack-tip element for modelling arbitrary crack propagations. *Theoretical and Applied Fracture Mechanics*, 105, Article 102422. <https://doi.org/10.1016/j.tafmec.2019.102422>

Important note

To cite this publication, please use the final published version (if applicable). Please check the document version above.

Copyright

Other than for strictly personal use, it is not permitted to download, forward or distribute the text or part of it, without the consent of the author(s) and/or copyright holder(s), unless the work is under an open content license such as Creative Commons.

Takedown policy

Please contact us and provide details if you believe this document breaches copyrights. We will remove access to the work immediately and investigate your claim.

Green Open Access added to TU Delft Institutional Repository

'You share, we take care!' - Taverne project

<https://www.openaccess.nl/en/you-share-we-take-care>

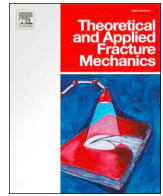
Otherwise as indicated in the copyright section: the publisher is the copyright holder of this work and the author uses the Dutch legislation to make this work public.



ELSEVIER

Contents lists available at ScienceDirect

Theoretical and Applied Fracture Mechanics

journal homepage: www.elsevier.com/locate/tafmec

A crack-tip element for modelling arbitrary crack propagations

Qiang Fu^a, Sinan Yi^b, Boyang Chen^c, Tinh Quoc Bui^{d,e}, Xiaofei Hu^{a,*}, Weian Yao^{a,*}^a State Key Laboratory of Structural Analysis for Industrial Equipment, International Center for Computational Mechanics, Dalian University of Technology, Dalian 116024, PR China^b Beijing Institute of Mechanical and Electrical Engineering, Beijing 100074, PR China^c Faculty of Aerospace Engineering, Delft University of Technology, Kluyverweg 1, 2629 HS Delft, the Netherlands^d Institute for Research and Development, Duy Tan University, Da Nang City, Viet Nam^e Department of Civil and Environmental Engineering, Tokyo Institute of Technology, 2-12-1-W8, Ookayama, Meguro-ku, Tokyo 152-8552, Japan

ARTICLE INFO

Keywords:

Floating node method

SASE

Crack propagation

Stress intensity factor

ABSTRACT

Numerical study on crack propagation are of great importance for structure design and assessment. In this contribution, the floating node method (FNM) is combined with the symplectic analytical singular element (SASE) to form a new crack-tip element. The four node quadrilateral crack-tip element contains a SASE for the crack tip area to account for the singularity issue. Floating nodes are used to form a smooth transition mesh to fill the other area of the element automatically once the SASE has been generated. Delaunay triangulation is used to guarantee the quality of the transition elements. Strong discontinuity resulted from complex crack networks with multiple cracks is treated by the FNM. Criteria for crack nucleation, propagation angle and length of new crack segment are given. Interaction between cracks and between crack and defect can be readily modelled without any prior knowledge of crack path. The fracture process of crack propagation can be modelled without remeshing. Inherited from the FNM, the proposed crack-tip element is especially suitable to be implemented in the form of a user defined element. Completed fracture processes with crack nucleation, propagation and interaction are modelled in the numerical examples.

1. Introduction

Cracks due to defects, repair, corrosion or other reasons arise frequently in engineering applications, and it may significantly reduce fatigue life of the structure or even lead to catastrophic failure. With the development of computational methods for fracture, numerical modelling has emerged as a powerful tool in engineering practices to aid the design against failure. Due to the existence of strong discontinuity and the singularity issue in crack problems, special numerical methods such as enriched elements and crack-tip elements are needed to efficiently and effectively model these problems.

For the modelling of arbitrary crack propagations, continuous remeshing is generally required in conventional finite element method (FEM) and the modelling is time-consuming as a result. Although extensive efforts were devoted, this problem was not solved satisfactorily until the emergence of the Extended Finite Element Method (XFEM) [1]. In XFEM, the use of Heaviside enrichment allows a crack within an element to be represented without remeshing. In this way, modelling of crack propagations can be conducted on a fixed regular mesh. Since developed, XFEM has drawn extensive attentions and has been adopted

for various crack problems such as bimaterial interface crack [2], three-dimensional (3D) crack [3–8], cohesive crack [9–11], fatigue crack growth [12], fracture of structures with complex geometry [13], failure of composite material [14–16], kinked crack [17], crack propagation in the material with micro defects [18], etc. A popular variant of XFEM, namely Phantom Node Method (PNM), is essentially equivalent to XFEM with only the Heaviside enrichment [19]. In PNM, strong discontinuity is represented by activating additional phantom nodes and forming overlapping sub-elements with partial integration domains [20–22]. The nodal Degree-of-Freedoms (DoFs) of the PNM are compatible with those of conventional elements and hence it can be readily implemented into a standard finite element code. PNM has been further developed in numerous studies for modelling of cohesive cracks [23–25], 3D cracks [26], failure in composite laminates [27–29], dynamic crack problems [30], and other fracture problems [31–33]. Based on the development of XFEM and PNM, the floating node method (FNM) was proposed where additional nodes are introduced for the representation of discontinuity in an element [34]. Unlike in PNM, the locations of additional nodes do not need to be fixed. They are moved to the crack-edge intersections to form fully-integrated sub-elements.

* Corresponding authors at: State Key Laboratory of Structural Analysis for Industrial Equipment, Dalian, PR China.

E-mail addresses: hxf@dlut.edu.cn (X. Hu), ywa@dlut.edu.cn (W. Yao).

<https://doi.org/10.1016/j.tafmec.2019.102422>

Received 18 September 2019; Received in revised form 28 October 2019; Accepted 18 November 2019

Available online 27 November 2019

0167-8442/ © 2019 Elsevier Ltd. All rights reserved.

Complex crack networks with multiple cracks in an element can be represented directly by forming sub-elements that are conforming to the cracks. So far, applications of FNM on fracture problems have been reported in numerous publications, ranging from single-crack to many-crack problems on isotropic and composite materials [35–45].

For brittle fracture, the analytical solution under Linear Elastic Fracture Mechanics (LEFM) indicates that the stress field is singular in the vicinity of the crack tip. A general approach in FEM for considering the singularity issue is using the crack-tip element. The earliest crack-tip elements are the quarter point singular element [46] and the enriched element [47]. The singular stress fields around the crack tip can be reproduced in the crack-tip elements and the mixed-mode stress intensity factors (SIFs) can be calculated through a post-processing such as the J-integral. A more representative example of the crack-tip element is XFEM [1], in which the displacement field in the crack-tip element is defined by a mix of standard Lagrange shape functions and the eigen solution (Irwin's solution) of the crack problem with low order terms. Menouillard et al., investigated the enrichment strategy for XFEM in dealing with dynamic crack propagation [48], Bayesteh and Mohammadi studied the effect of crack tip enrichment functions in XFEM for plate and shell structures [49], Bouhala et al., proposed an XFEM enrichment for the crack terminating at a bimaterial interface [50], Song and Wolf proposed a special enrichment scheme by using a scaled boundary finite element method (SBFEM) [51,52]. Kumar et al., proposed crack tip enrichment schemes for dynamic crack problem under blast loading and ductile crack problem, only a few additional DoFs are added to the crack tip nodes which slightly increases the computational cost [53,54]. Although in many studies only low order terms of the eigen solution of the crack problem are used, it is found that an enrichment with higher order terms can improve the solving accuracy as stated in the studies of Karihaloo and Xiao [55,56]. Similar conclusions can also be found in Refs. [57–59]. In the previous studies, Hu proposed a series of crack-tip elements in which the physical fields are defined purely by the eigen solutions where not only the singular terms but also the higher order terms are employed. Due to the fact that the eigen solutions are solved by using a symplectic analytical approach, this type of element is termed as “symplectic analytical singular element (SASE)”. The SASE has been applied for many basic crack problems such as, general cracks [60], fatigue crack growth [61,62], bimaterial crack [63,64], viscoelastic cracks [65], thermal conduction for crack [66,67], dynamic crack problem [68] and cohesive cracks [69]. The solving accuracy and stability of the SASEs have been shown to be highly satisfactory. With the SASEs, fracture parameters such as SIFs and heat flux intensity factors (HFIFs) can be calculated accurately without mesh refinement around the crack tip or any post-processing. However, the SASEs would require remeshing when dealing with crack propagation problems [61,62], making the models computationally expensive.

2. Motivation

The purpose of this work is to enhance the SASE method by combining it with an enriched element technology for handling crack propagations without remeshing. Due to the flexibility of assigning additional (floating) nodes in elements, the ease of handling different types of discontinuities and the stability of the sub-elements thanks to their full-domain integration, FNM is chosen as the candidate for this purpose. Subjected to external loadings and constraints, the original crack propagates and forms the new crack surfaces Γ_{new} and a new crack tip as shown in Fig. 1. In dealing with the crack problem by using numerical methods such as the conventional FEM, it is faced with two main challenges. The first one is the discontinuous fields across the new crack surfaces (also known as the strong discontinuity). It therefore requires the remeshing technique to fit to each new crack segments. The other challenge is the crack tip singularity issue. According to LEFM, the value of stresses approach infinite at the vicinity of a crack tip. In this study, the SASE is combined with FNM for crack propagation in two-

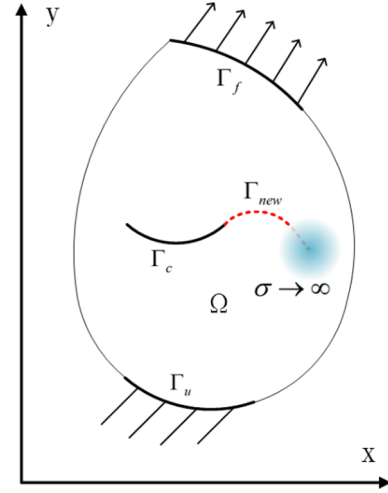


Fig. 1. A cracked two dimensional domain with arbitrary shape.

dimensional (2D) domain. The crack tip area is occupied by using a SASE to describe the singular stress field accurately. The FNM is used to treat the strong discontinuity. Additional floating nodes are assigned to the new crack surfaces to fit to the changing crack geometry during propagation. Meanwhile, floating nodes are also assigned to the SASE around the moving crack tip to form a smooth transition mesh with the surrounding regular elements. The assignments of additional floating nodes are conducted automatically such that remeshing can be eliminated with the proposed method. Taking advantages of each method, the singular stress fields at the crack tips can be modelled accurately and crack propagations handled efficiently. A few numerical examples are given to verify and validate the proposed method.

After defining the discussed problem with the basic equations in Section 3, the two main aspects of the proposed method are discussed in Section 4 for the strong discontinuity and Section 5 for the singularity issue. The combination of the FNM and the SASE is also discussed in Section 5. The solving procedure, criteria and other relevant aspects are discussed in Section 6. A few representative numerical examples are provided in Section 7, and a conclusion is given in Section 8.

3. Basic equations

Let consider a cracked two-dimensional (2D) plate as shown in Fig. 1, the relationship between stress and displacement under plane stress assumption is specified by

$$\begin{aligned}\sigma_r &= \frac{E}{1-\nu^2} \left[\frac{\partial u_r}{\partial r} + \frac{\nu}{r} \left(u_r + \frac{\partial u_\theta}{\partial \theta} \right) \right] \\ \sigma_\theta &= \frac{E}{1-\nu^2} \left[\frac{1}{r} \left(u_\theta + \frac{\partial u_\theta}{\partial \theta} \right) + \nu \frac{\partial u_r}{\partial r} \right] \\ \tau_{r\theta} &= \frac{E}{2(1+\nu)} \left(\frac{\partial u_\theta}{\partial r} - \frac{u_\theta}{r} + \frac{1}{r} \frac{\partial u_r}{\partial \theta} \right)\end{aligned}\quad (1)$$

where (r, θ) is the polar coordinate system. The notations σ_r , σ_θ and $\tau_{r\theta}$ represent stress components. u_r and u_θ are displacement components along the r -axis and θ -axis, respectively. E and ν are Young's modulus and Poisson's ratio, respectively. The stress equilibrium equations are given by

$$\begin{aligned}\frac{\partial \sigma_r}{\partial r} + \frac{1}{r}(\sigma_r - \sigma_\theta) + \frac{1}{r} \frac{\partial \tau_{r\theta}}{\partial \theta} + F_1 &= 0 \\ \frac{\partial \tau_{r\theta}}{\partial r} + \frac{2}{r} \tau_{r\theta} + \frac{1}{r} \frac{\partial \sigma_\theta}{\partial \theta} + F_2 &= 0\end{aligned}\quad (2)$$

where F_1 and F_2 are body forces. The boundary conditions at the crack surfaces are

$$\sigma_\theta = \hat{\sigma}_\theta(r), \quad \tau_{r\theta} = \hat{\tau}_{r\theta}(r), \quad \text{at } \Gamma_c \quad (3)$$

where $\hat{\sigma}_\theta(r)$ and $\hat{\tau}_{r\theta}(r)$ are prescribed.

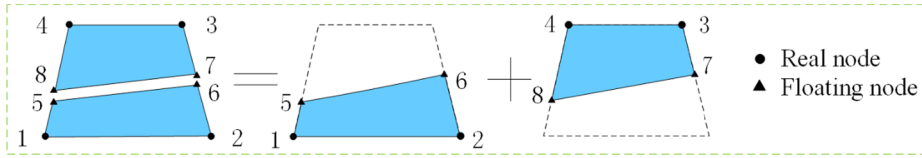


Fig. 2. Representation of strong discontinuity in an element by using the floating node method.

4. Strong discontinuity and floating node method

Let consider an element which is cut through by a crack segment as shown in the left sub-figure of Fig. 2, the strong discontinuity formed by the crack is treated by using the floating node method (FNM) [34,37]. In the FNM, additional floating nodes are introduced which are moved to the two ends of the crack if an element is cut through as shown in Fig. 2. The formed two sub-elements are

$$\text{Element \#1: } 1, 2, 6, 5, \text{ Element \#2: } 8, 7, 3, 4 \quad (4)$$

The formed two sub-elements are still standard elements and their formulations are

$$P_1 = K_1 d_1, \quad P_2 = K_2 d_2 \quad (5)$$

where $d_1 = [u_1, v_1, u_2, v_2, u_6, v_6, u_5, v_5]^T$ and $d_2 = [u_8, v_8, u_7, v_7, u_3, v_3, u_4, v_4]^T$ are the nodal displacement vectors of the two sub-elements, P_1 and P_2 are the nodal force vectors, K_1 and K_2 are the stiffness matrix. Hence, the integration of the stiffness matrix of the sub-elements are conducted following the standard Gauss quadrature schemes on their domains. Assembling the stiffness matrix as well as the nodal force vector into the global FEM system, the crack problem can be solved. For cases where the sub-element is a polygon, it can be partitioned into a few standard elements. For cases where an element is cut through by multiple cracks, it is only required to arrange the nodal connectivity arrays properly to form the corresponding sub-elements that conform with the crack boundaries. Different scenarios of crack interaction in an element and the arrangement of node connectivity are shown in Fig. 3, indicating the generality of the method. More details about the FNM and the comparison among FNM, XFEM and PNM are referred to Refs.[34]. More applications of the FNM are referred but not limited to Refs. [35,36,40]. The FNM is employed for the strong discontinuity in the present study for modelling crack propagation.

5. Singularity issue and a crack-tip element

5.1. Eigen solution of the crack problem

The analytical solution of a crack problem in the domain $\Omega: \{0 \leq r \leq \infty; -\pi \leq \theta \leq \pi\}$ is normally investigated under the polar coordinate system (r, θ) as shown in Fig. 4. The 2D elasticity problem can be transformed from Lagrangian system into Hamiltonian system [70]. For that purpose, the following generalized variables should be introduced

$$\xi = \ln r, \quad S_r = r\sigma_r, \quad S_\theta = r\sigma_\theta, \quad S_{r\theta} = r\tau_{r\theta}. \quad (6)$$

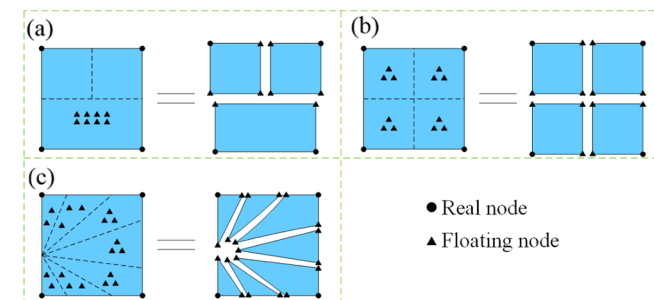


Fig. 3. Representation of interaction of cracks by using the floating node method. (a) A T shaped crack [34], (b) two crossing cracks, (c) six cracks [40].

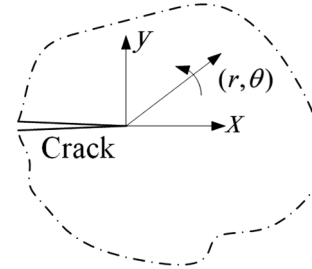


Fig. 4. Illustration of a crack under the polar coordinate system.

where ξ is essentially a generalized coordinate and S_r, S_θ and $S_{r\theta}$ are generalized stresses. With the generalized variables, the two-field (stress and displacement) Hellinger-Reissner (H-R) variational principle of plane stress problem can be expressed as

$$\delta \int_{-\pi}^{\pi} \int_0^{\infty} \left\{ S_r \frac{\partial u_r}{\partial \xi} + S_\theta \left(\frac{\partial u_\theta}{\partial \theta} + u_r \right) + S_{r\theta} \left(\frac{\partial u_\theta}{\partial \xi} - u_\theta + \frac{\partial u_r}{\partial \theta} \right) - \frac{1}{2E} [S_\theta^2 + S_r^2 - 2\nu S_r S_\theta + 2(1 + \nu) S_{r\theta}^2] \right\} d\xi d\theta = 0 \quad (7)$$

The variation of the functional in Eq. (7) for an arbitrary change δS_θ gives the following relationship

$$S_\theta = E \left(u_r + \frac{\partial u_\theta}{\partial \theta} \right) + \nu S_r \quad (8)$$

Substituting S_θ back into Eq. (7) transforms the H-R variational principle into

$$\delta \int_{-\pi}^{\pi} \int_0^{\infty} \left\{ S_r \frac{\partial u_r}{\partial \xi} + \nu S_r \left(u_r + \frac{\partial u_\theta}{\partial \theta} \right) + S_{r\theta} \left(\frac{\partial u_\theta}{\partial \xi} + \frac{\partial u_r}{\partial \theta} - u_\theta \right) + \frac{E}{2} \left(u_r + \frac{\partial u_\theta}{\partial \theta} \right)^2 - \frac{1}{2E} [(1 - \nu^2) S_r^2 + 2(1 + \nu) S_{r\theta}^2] \right\} d\xi d\theta = 0 \quad (9)$$

There are four independent variables in the new variational principle and they are termed as the configuration variables (u_r and u_θ) and the dual variables (S_r and $S_{r\theta}$). The variation of the functional in Eq. (9) for arbitrary changes of $\delta u_r, \delta u_\theta, \delta S_r$ and $\delta S_{r\theta}$ gives a first order differential equation set

$$\frac{\partial Z}{\partial \xi} = HZ \quad (10)$$

where $Z = [u_r, u_\theta, S_r, S_{r\theta}]^T$. It is proven that H is a Hamiltonian operator matrix, it is specified by

$$H = \begin{bmatrix} -\nu & -\nu \frac{\partial}{\partial \theta} & \frac{1-\nu^2}{E} & 0 \\ -\frac{\partial}{\partial \theta} & 1 & 0 & \frac{2(1+\nu)}{E} \\ E & E \frac{\partial}{\partial \theta} & \nu & -\frac{\partial}{\partial \theta} \\ -E \frac{\partial}{\partial \theta} & -E \frac{\partial^2}{\partial \theta^2} & -\nu \frac{\partial}{\partial \theta} & -1 \end{bmatrix} \quad (11)$$

By means of separation of variables, the solution of Z is considered to take the form $Z = \exp(\mu\xi)\psi(\theta)$ where μ and ψ are eigenvalue and the corresponding eigenvector. The eigenvector is given by $\psi = [\varphi_u(\theta), \varphi_v(\theta), \varphi_r(\theta), \varphi_{r\theta}(\theta)]^T$ in which $\varphi_u(\theta), \varphi_v(\theta), \varphi_r(\theta)$ and $\varphi_{r\theta}(\theta)$ are displacements and generalized stresses after separation of variable. A similar notation $\varphi_\theta(\theta)$ is used for S_θ in the rest of the paper. Substituting Z back into Eq. (10), the problem is transformed into an eigenvalue problem

$$(\mathbf{H} - \mu I)\psi(\theta) = 0 \tag{12}$$

The eigenvalue can be solved by letting $\det(\mathbf{H} - \mu I) = 0$ and the analytical solutions are specified by

$$\mu = \frac{n}{2}, n = 0, 1, 2, 3, \dots \text{ (double root)} \tag{13}$$

Substituting the eigenvalues back into Eq. (12), the corresponding eigenvectors can be solved with the traction free condition at the crack surfaces

$$E\left(u_r + \frac{\partial u_\theta}{\partial \theta}\right) + \nu S_r = 0, \quad S_{r\theta} = 0, \quad \theta = \pm\pi \tag{14}$$

It is noteworthy that all the eigenvalues are double roots, and it can be proven that there are two independent eigenvectors corresponding to an eigenvalue. One of them represents symmetric deformation while the other one anti-symmetric deformation. For zero eigenvalue, the eigenvectors are given by

$$\psi_s^{(1)} = [\cos \theta \quad -\sin \theta \quad 0 \quad 0]^T, \quad \varphi_{\theta,s}^{(1)}(\theta) = 0 \tag{15}$$

$$\psi_a^{(2)} = [\sin \theta \quad \cos \theta \quad 0 \quad 0]^T, \quad \varphi_{\theta,a}^{(2)}(\theta) = 0 \tag{16}$$

The subscripts “s” and “a” represent symmetric and anti-symmetric deformations, respectively. The general solutions of the eigenvectors corresponding to nonzero eigenvalue are specified by

$$\psi_s^{(j)} = \begin{bmatrix} A_u \cos(1 + \mu)\theta + C_u \cos(1 - \mu)\theta \\ A_v \sin(1 + \mu)\theta + C_v \sin(1 - \mu)\theta \\ A_r \cos(1 + \mu)\theta + C_r \cos(1 - \mu)\theta \\ A_{rs} \sin(1 + \mu)\theta + C_{rs} \sin(1 - \mu)\theta \end{bmatrix}, \quad j = 3, 5, 7, \dots \tag{17}$$

$$\varphi_{\theta,s}^{(j)}(\theta) = A_s \cos(1 + \mu)\theta + C_s \cos(1 - \mu)\theta, \quad j = 3, 5, 7, \dots \tag{18}$$

$$\psi_a^{(j+1)} = \begin{bmatrix} B_u \sin(1 + \mu)\theta + D_u \sin(1 - \mu)\theta \\ B_v \cos(1 + \mu)\theta + D_v \cos(1 - \mu)\theta \\ B_r \sin(1 + \mu)\theta + D_r \sin(1 - \mu)\theta \\ B_{rs} \cos(1 + \mu)\theta + D_{rs} \cos(1 - \mu)\theta \end{bmatrix}, \quad j = 3, 5, 7, \dots \tag{19}$$

$$\varphi_{\theta,a}^{(j+1)}(\theta) = B_s \sin(1 + \mu)\theta + D_s \sin(1 - \mu)\theta, \quad j = 3, 5, 7, \dots \tag{20}$$

where the explicit expressions of the 20 coefficients A_u, B_u, C_u, \dots are referred to [60,70]. The analytical solution to the original problem can be expressed in terms of an eigen expansion

$$\mathbf{Z} = \sum_{j=1}^{\infty} a_j e^{\xi \mu^{(j)}} \psi^{(j)}(\theta) \tag{21}$$

where the superscript j indicates the j th eigen expanding term and a_j is the expanding coefficient.

5.2. Formulation of a circular singular element [60]

In the construction of a singular element, the eigen expansion (21) with the unknown expanding coefficients is the best choice to define the fields around the crack tip since the singular terms (3 and 4) and other higher order terms are included. A circular singular element termed as the SASE (as illustrated in Fig. 5) which is constructed in this way is available in [60], and its formulation is briefly listed here. In practice, Eq. (21) is truncated to include finite numbers of the expanding terms

$$\mathbf{Z} = \sum_{j=1}^M a_j e^{\xi \mu^{(j)}} \psi^{(j)} \tag{22}$$

Rewriting it in form of matrix gives

$$\mathbf{p} = [u_r, u_\theta]^T = \Phi \mathbf{A} \mathbf{a}, \quad \mathbf{q} = [S_r, S_{r\theta}]^T = \Theta \mathbf{A} \mathbf{a} \tag{23}$$

where $\mathbf{a} = [a_1, a_2, \dots, a_M]^T$ is the vector of the unknown expanding coefficients. Substituting Eq. (23) back into Eq. (9) makes the only

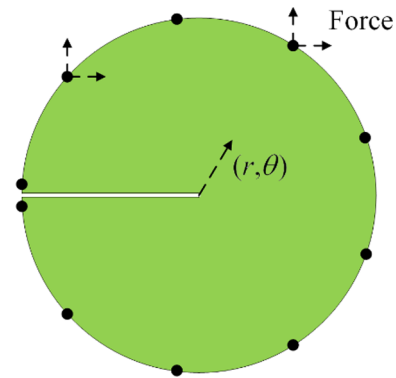


Fig. 5. Schematic illustration of the circular singular element.

independent function be a in the variational principle. In view of the fact that the eigen functions have satisfied all the interior fundamental equations and the crack surface boundary conditions, the variational principle can be simplified into

$$\delta \int_{-\pi}^{\pi} \frac{1}{2} (p^T q) \Big|_{\xi=\ln \rho} d\theta = 0 \tag{24}$$

The variational principle can be rewritten in form of matrix

$$\delta \left(\frac{1}{2} a^T \mathbf{A}^T \mathbf{R} \mathbf{A} a \Big|_{\xi=\ln \rho} \right) = 0 \text{ where } \mathbf{R} = \int_{-\pi}^{\pi} \Phi^T \Theta d\theta \tag{25}$$

Denoting $\mathbf{d} = [u_{r,1}, u_{\theta,1}, \dots, u_{\theta,N}]^T$ the nodal displacement vector, the relationship between the eigen expanding coefficients and the nodal displacement is given by

$$\mathbf{d} = \mathbf{T} \mathbf{B} \mathbf{a} \text{ or } \mathbf{a} = \mathbf{B}^{-1} \mathbf{T}^{-1} \mathbf{d} \tag{26}$$

where $\mathbf{B} = \mathbf{A}(\xi = \ln \rho)$ and the matrix

$$\mathbf{T} = \begin{bmatrix} \varphi_u^{(1)}(\theta_1), \varphi_u^{(2)}(\theta_1), \varphi_u^{(3)}(\theta_1), \dots, \varphi_u^{(2N)}(\theta_1) \\ \varphi_v^{(1)}(\theta_1), \varphi_v^{(2)}(\theta_1), \varphi_v^{(3)}(\theta_1), \dots, \varphi_v^{(2N)}(\theta_1) \\ \dots \\ \varphi_v^{(1)}(\theta_N), \varphi_v^{(2)}(\theta_N), \varphi_v^{(3)}(\theta_N), \dots, \varphi_v^{(2N)}(\theta_N) \end{bmatrix} \tag{27}$$

In order to ensure that \mathbf{T} is a square matrix, $2N$ expanding terms are selected in Eq. (22) (i.e., $M = 2N$) if N nodes are used in the singular element. In this way, the fields of displacement and the generalized stress can be represented by using the nodal values of displacement as in standard elements

$$[u_r, u_\theta]^T = \Phi \mathbf{A} \mathbf{B}^{-1} \mathbf{T}^{-1} \mathbf{d} \tag{28}$$

$$[S_r, S_{\theta}]^T = \Theta \mathbf{A} \mathbf{B}^{-1} \mathbf{T}^{-1} \mathbf{d} \tag{29}$$

Essentially, $\Phi \mathbf{A} \mathbf{B}^{-1} \mathbf{T}^{-1}$ is the standard shape function which relates the displacement field with the nodal values of displacement. At least three differences between the SASE and the XFEM can be found from the definition of the shape function. (1) both of displacement and stress (stress can be calculated with the generalized stress) are defined with shape functions directly in the SASE. This is different from XFEM in which only displacement is defined with shape function while the stress is calculated from the spatial gradient of the displacement. (2) The SASE employs many nodes on which the DoFs are just standard displacement components. On the contrary, the XFEM uses less nodes but extra DoFs are introduced on these nodes. It makes the D.O.Fs being physically meaningless. (3) Higher order eigen expanding terms besides the low order singular terms are employed in the definition of the SASE, it is known that the benefit by doing this is that the size of the element can be even bigger for the required accuracy [64]. In the early version of XFEM in which only singular terms are included, refined mesh should be used to get a satisfactory prediction.

Based on the obtained relationship, the variational principle can be rewritten as

$$\delta \left(\frac{1}{2} \mathbf{d}^T \mathbf{T}^{-T} \mathbf{R} \mathbf{T}^{-1} \mathbf{d} \right) = 0 \quad (30)$$

Hence, the stiffness matrix is of the singular element

$$\mathbf{K}_s = \mathbf{T}^{-T} \mathbf{R} \mathbf{T}^{-1} \quad (31)$$

Although the finite element formulation is derived under the polar coordinate system, it should be transformed into the Cartesian coordinate system to match to the regular elements which are normally derived under the Cartesian coordinate system. The coordinate transformation technique is readily available in most finite element books, it is not introduced here.

5.3. Formulation of a new regular shaped crack-tip element

Considering the singularity issue around the crack tip, one has to insert the circular singular element around the crack tip. However, the irregular shape of the circular singular element has brought difficulties in modelling crack propagation with a regular mesh. For this reason, a four-node crack-tip element is formulated to have better compatibility when modelling on a fixed regular mesh. The new crack-tip element contains a circular singular element in the center and some other regular sub-elements in the transition domain as shown in Fig. 6. The singular element and the regular elements are formed with the existing four real nodes and additional floating nodes assigned to the element in the preprocessing. Delaunay triangulation is used to partition the transition domain to ensure the quality of the sub-elements. A shared source code for the implementation of Delaunay triangulation is employed in this study [71]. Once the position of the circular singular element is determined (see Section 6.2), the topological configuration of the transition area is obtained as well. The right sub-figure of Fig. 6 depicts the triangle sub-elements. In fact, other meshing strategies can also be used to generate quadrilateral sub-elements in the transition area. The meshing process generates a set of local node numbers which should be related to the real and floating nodes assigned to the element. It is noted that all the floating nodes on the edges except the two on the crack segment are eliminated by multiple point constraint (MPC). The formulation of the new crack-tip element is obtained by assembling the stiffness matrix as well as the force vectors of the sub-elements and the singular element

$$\mathbf{K}_{el} = \aleph(\mathbf{K}_s, \mathbf{K}_1, \mathbf{K}_2, \mathbf{K}_3, \dots) \quad (32)$$

$$\mathbf{P}_{el} = \aleph(\mathbf{P}_1, \mathbf{P}_2, \mathbf{P}_3, \dots) \quad (33)$$

where \aleph is the assembly operator. The force vector of the singular element is zero if the domain is free from external loading such as crack surface traction. Otherwise, the force vector of the singular element should be calculated and assembled. Just like in other adaptive mesh refinement techniques, hanging nodes are generated at the edges of the four-node singular element as shown in Fig. 6. In this study, the hanging nodes are constrained to the two real nodes of the edge through the means of MPC.

$$\mathbf{d}_{han} = \mathbf{T}_{mpc} \mathbf{d}_r \quad (34)$$

where \mathbf{d}_{han} is the vector of the hanging nodes and \mathbf{d}_r is the vector of the real and the rest floating nodes. \mathbf{T}_{mpc} is the transformation matrix. The formulation of the crack-tip element should be updated

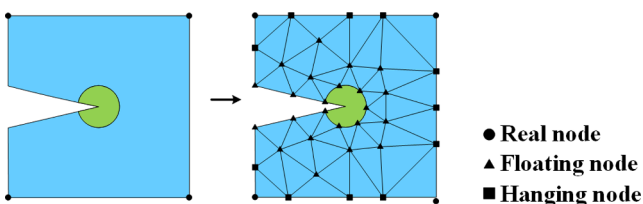


Fig. 6. Schematic illustration of a four-node crack-tip element.

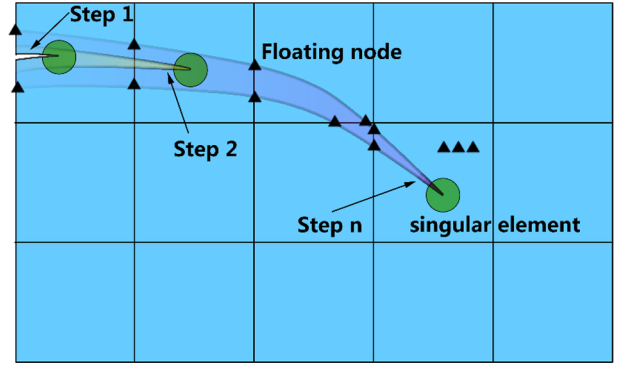


Fig. 7. Illustration of the solving procedure with the crack-tip element.

$$\mathbf{K}_{el}^{new} = \mathbf{T}_{mpc}^T \mathbf{K}_{el} \mathbf{T}_{mpc} \quad (35)$$

$$\mathbf{P}_{el}^{new} = \mathbf{T}_{mpc}^T \mathbf{P}_{el} \quad (36)$$

6. Discussions

6.1. Solving procedure

For a quasi-static problem, the external loading is cut into several increments ΔP_g . The following equation is solved at each load increment

$$\mathbf{d}_g = \mathbf{K}_g^{-1}(\mathbf{u})(\mathbf{P}_g + \Delta \mathbf{P}_g) \quad (37)$$

where $\mathbf{K}_g(\mathbf{u})$ is the global stiffness matrix and it depends on the current configuration of the structure. \mathbf{d}_g and \mathbf{P}_g are global nodal displacement and force vector. For a cracked structure as shown in Fig. 7, a circular singular element is put at the original crack tip at “step 1” and the element becomes a crack-tip element. It is noteworthy that the transition elements as well as the floating nodes are hidden in the figure for a clear illustration. With the increment of external loading, the crack propagates into the next element at “step 2” and the element becomes a crack-tip element. After a few loading increments, the crack enters an element far away at “step n” as shown in Fig. 7 and several elements are cut through by the crack during the crack propagation process. The element is cut through when the crack tip leaves it, and only a few floating nodes are left to represent the strong discontinuity using the FNM discussed in Section 4 and it is illustrated by the crack trajectory of “step n” in Fig. 7.

6.2. Length of the new crack segment

In the numerical modelling, crack propagation trajectory is composed of several consecutive segments. Each crack segment is a straight line which links the old and the new crack tips. When the direction of a new crack segment is determined, its length must also be determined. In order to guarantee the quality of the mesh inside the proposed regular shaped crack-tip element, the new crack tip should be placed properly to keep it away from the edges of an element. A simple method is introduced to find the proper area for quadrilateral element. For other elements, such a proper area can also be found with a similar method. Generally, a quadrilateral element has two inscribed circles with three edges as shown in Fig. 8(a). The extension of the upper and lower edge of the element intersect at the point 5 and form an angle. The origins of the two inscribed circles must locate on the angular bisector of the angle, and their radius R_1 and R_2 can be determined. The origins of the two inscribed circles form a path (red line), and all the circles origin at the red line form the green area (note that part of the green area is overlapped by the pink area) shown in Fig. 8(a). Shrinking the radii of the two inscribed circles of the green area with a parameter k such that

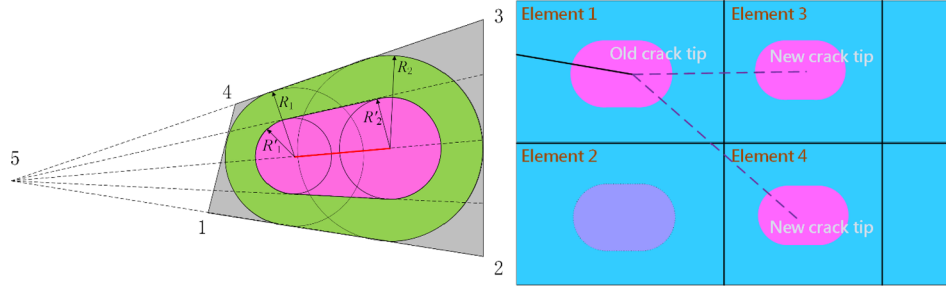


Fig. 8. (a) Proper area of the new crack tip, (b) choosing the length of new crack segment.

$$\frac{R'_1}{R_1} = \frac{R'_2}{R_2} = k, \quad k = 0.7 \text{ is chosen in this paper} \quad (38)$$

gives a pair of smaller radii R'_1 and R'_2 . Making two circles origin at the two ends of the red line with R'_1 and R'_2 further forms the pink area in the figure which is considered as the proper area for the new crack tip.

A stepwise procedure for choosing the length of a new crack segment is provided as follows. For the elements in the area around the old crack tip as shown in Fig. 8(b), the crack tip proper area should be determined during the modelling. There are mainly two typical cases in choosing the proper crack segment length. In case 1, the crack tip moves from element #1 to the adjacent element #3 along a direction such that the crack tip can be put into the pink area. In case 2, the crack propagates from element #1 to element #2. However, one can find that there isn't a proper place along the potential crack path in element #2 to put the crack tip. In this case, the crack segment should be extended to element #4 in which the crack tip can be placed properly. Once the crack segment length is determined, the load increment ΔP_g for this step is adjusted such that the equivalent SIF (defined in Section 6.5) equals to the critical value. In practice, a trial value of the load increment $\Delta P'_g$ is used to get a temporary solution. The real value of ΔP_g and the solution can be scaled from the temporary solution with the ratio between the calculated SIF and the desired SIF. A flow chart of stepwise solving procedure is given in Fig. 9.

6.3. Fracture parameters

In the analytical solution (21), the first two expanding terms (zero eigenvalue) represent rigid body transitions along the x -axis and y -axis, respectively. These two terms have no contribution to the stresses. The third and fourth expanding terms are singular terms related to the eigenvalue $\mu = 1/2$, and the other expanding terms are higher order terms. In the limit of r going to zero, contributions from the higher order terms are negligible and the stresses are expressed as

$$\sigma_r = \frac{S_r}{r} = a_3 r^{-1/2} \varphi_{r,s}^{(3)}(\theta) + a_4 r^{-1/2} \varphi_{r,a}^{(4)}(\theta) \quad (39)$$

$$\tau_{r\theta} = \frac{S_{r\theta}}{r} = a_3 r^{-1/2} \varphi_{r,s}^{(3)}(\theta) + a_4 r^{-1/2} \varphi_{r,a}^{(4)}(\theta) \quad (40)$$

$$\sigma_\theta = \frac{S_\theta}{r} = a_3 r^{-1/2} \varphi_{\theta,s}^{(3)}(\theta) + a_4 r^{-1/2} \varphi_{\theta,a}^{(4)}(\theta) \quad (41)$$

In fracture mechanics, an standard definition of the SIFs is given by

$$K_I = \lim_{r \rightarrow 0} \sqrt{2\pi r} \sigma_\theta(\theta = 0), \quad K_{II} = \lim_{r \rightarrow 0} \sqrt{2\pi r} \tau_{r\theta}(\theta = 0) \quad (42)$$

From the above equations, the relationship between the SIFs and the expanding coefficients is given by

$$K_I = a_3 \sqrt{2\pi} (A_s + C_s) = a_3 E \sqrt{2\pi} \quad (43)$$

$$K_{II} = a_4 \sqrt{2\pi} (B_{rs} + D_{rs}) = -a_4 E \sqrt{2\pi} \quad (44)$$

It is seen that the SIFs K_I and K_{II} are proportional to the expanding

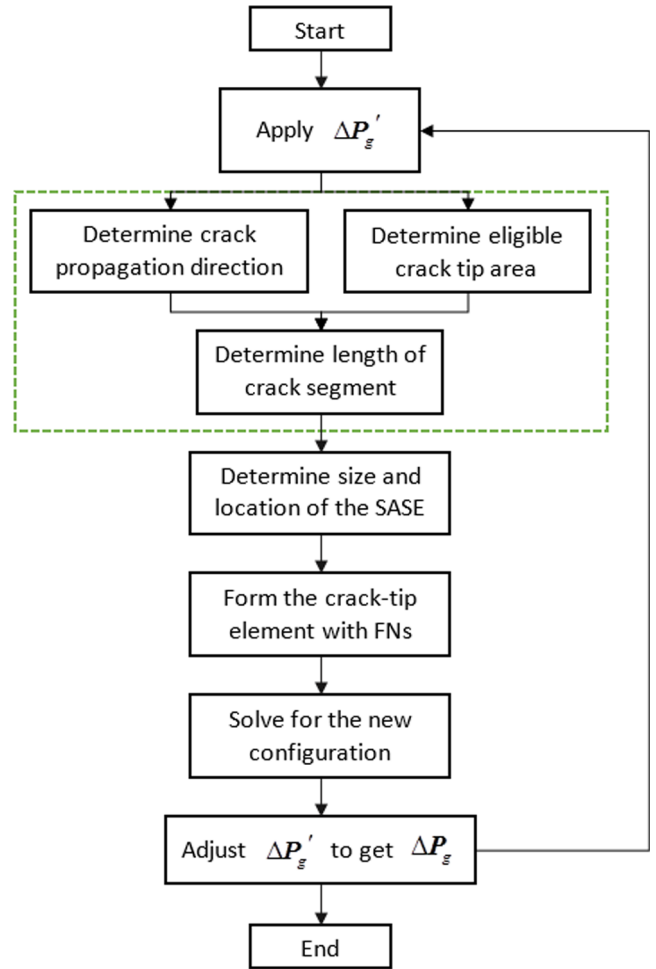


Fig. 9. Flow chart of the solving procedure.

coefficients a_3 and a_4 , respectively. The fifth expanding term $a_5 r \psi_s^{(5)}$ ($\mu = 1$) represents a constant transverse stress distribution parallel to the crack. It is essentially the well-known T-stress and it is proportional to a_5 . Now, it is clear that solving the values of the expanding coefficients plays a crucial role. In the most cases, they are solved numerically.

6.4. Crack nucleation criterion

For an intact material, a new crack is nucleated when the maximum principal stress reaches to the material tensile strength

$$\sigma_1 \geq S \quad (45)$$

The new crack is perpendicular to the direction of σ_1 , as shown in Fig. 10. In the absence of crack, the load increment ΔP_g is adjusted such

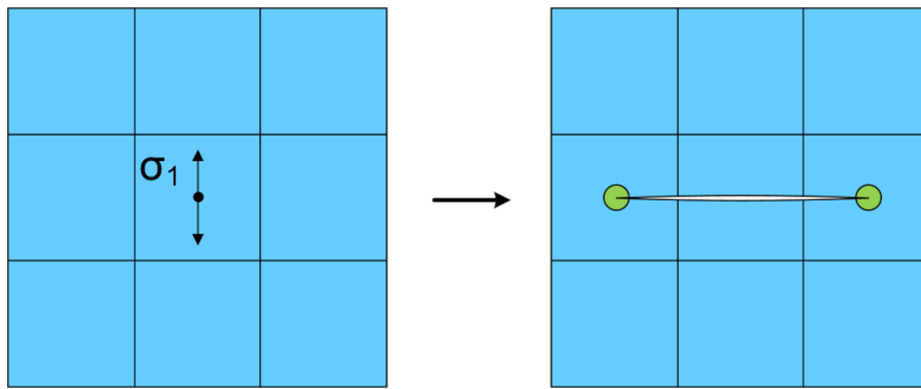


Fig. 10. Nucleation of crack.

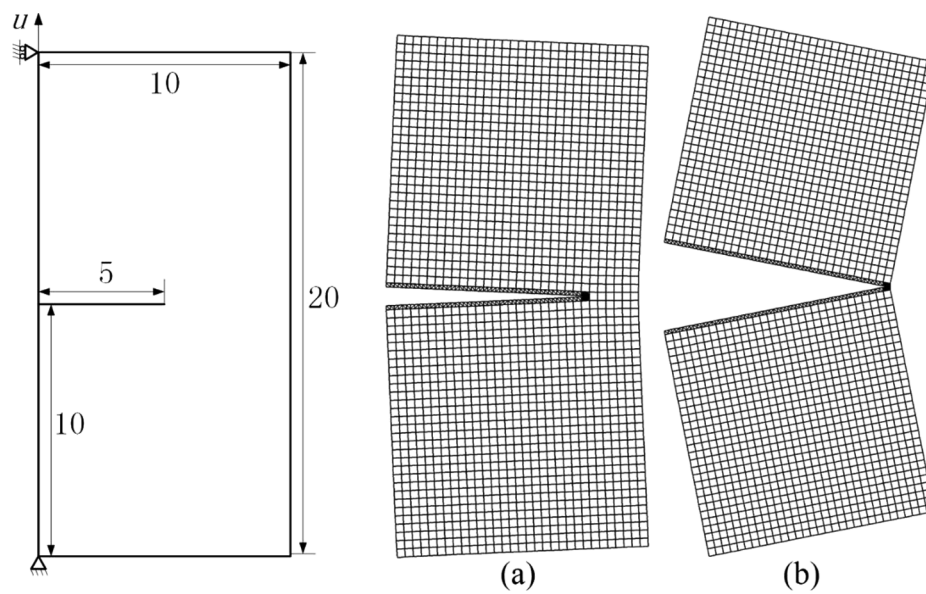


Fig. 11. Schematic illustration of an edge cracked plate (mm) subjected to mode I loading and the mesh during the modelling at (a) $u = 0.1591$ mm, (b) $u = 0.7852$ mm.

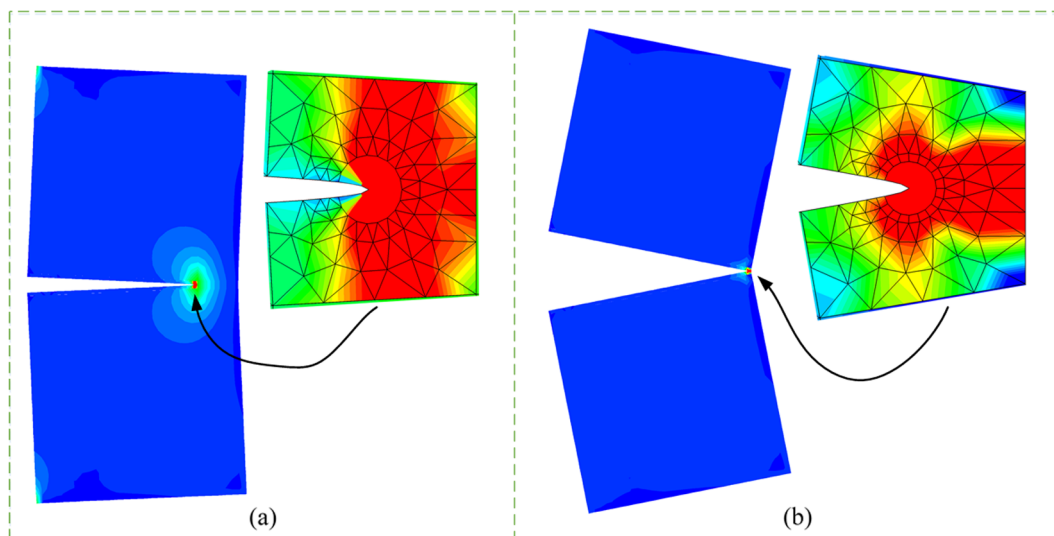


Fig. 12. Contours of the first principle stress and the interior meshes of the crack-tip element at (a) $u = 0.1591$ mm, (b) $u = 0.7852$ mm.

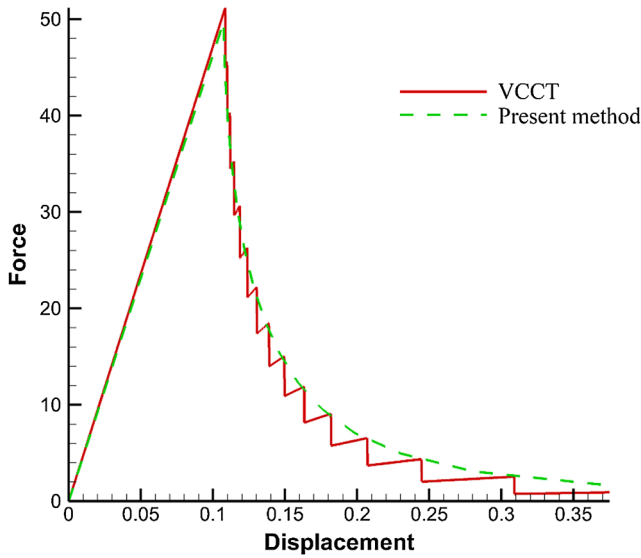


Fig. 13. Load-displacement curve of the mode I edge crack (mm).

that the maximum value of σ_1 of the structure is equal to S , and a new crack is then inserted in the element. In practice, an attempt value of ΔP_g is used to calculate the stresses. Since this step is linear elastic, the desired value of ΔP_g can be determined directly without iteration since it is proportional to the trial one, and the ratio is determined by the maximum value of σ_1 of the structure and S .

6.5. Crack propagation criterion

For an existing crack tip, the crack propagation angle θ_0 is calculated through the SIFs,

$$\theta_0 = 2 \arctan \frac{1}{4} \left(\frac{K_I}{K_{II}} \pm \sqrt{\left(\frac{K_I}{K_{II}} \right)^2 + 8} \right) \tag{46}$$

In this direction, the equivalent SIF K_{eff} is

$$K_{eff} = \cos \frac{\theta_0}{2} \left(K_I \cos^2 \frac{\theta_0}{2} - \frac{3}{2} K_{II} \sin \theta_0 \right) \tag{47}$$

The crack propagates if

$$K_{eff} \geq K_{IC} \tag{48}$$

where K_{IC} is the critical model I SIF which has the following relationship with the critical energy release rate

$$K_{IC} = \sqrt{EG_{IC}}, \text{ for plane stress} \tag{49}$$

$$K_{IC} = \sqrt{\frac{EG_{IC}}{1 - \nu^2}}, \text{ for plane strain} \tag{50}$$

7. Numerical examples

7.1. Edge crack (mode I)

An edge cracked plate as illustrated in the left sub-figure of Fig. 11 is investigated for the verification of the proposed method. The boundary condition and loading condition are also shown in Fig. 11. The Lamé constants $\lambda = 1.2 \times 10^4 \text{MPa}$, $\mu = 8 \times 10^3 \text{MPa}$ and the fracture energy $G_c = 1 \text{N/mm}$. The initial mesh of the plate has 1891 rectangular elements (isoparametric quadrilateral element). The plate is subjected to mode I loading condition, and the crack is anticipated to propagate along the original crack path. During the modelling, it is found that the absolute value of mode II SIF is negligible in comparison with mode I SIF. Hence the predicted crack propagation angle is always close to zero according to Eq. (46). As shown in the right sub-figures of Fig. 11, the predicted crack trajectory is a straight line indicating the modelling result is correct. The contours of the first principle stress over the whole plate at different loading stages are shown in Fig. 12(a) and (b), in which a clear stress concentration around the crack tip is observed. Besides, clear stress concentrations are also found at the locations of the applied boundary and loading conditions. These two stress concentrations are resulted by the computational model in which the loading and constraint are applied directly on the nodes. In practice, these two areas can be neglected when applying crack nucleation criterion. The local mesh of the proposed crack-tip element is also shown. Taking the advantage of Delaunay triangulation, the quality of the formed triangular elements is satisfactory.

For the extreme case where the crack tip is close to the boundary of the plate, other methods which use domain integral for the calculation of SIFs [43] may be limited since it is very hard to select a proper domain. The problem does not exist in the present method which does not require any post-processing for the calculation of the SIFs. As shown in Fig. 12(b), the mesh quality inside the proposed crack-tip element is still satisfactory. The predicted load–displacement curve is shown in Fig. 13, in which the result obtained by using VCCT [72] is also given for comparison. It is seen that the two methods agree well with each

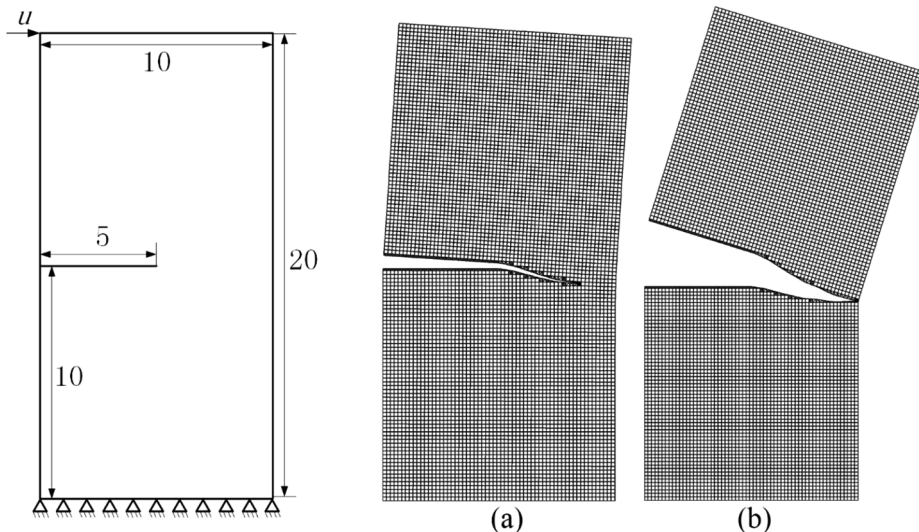


Fig. 14. Schematic illustration of an edge cracked plate (mm) subjected to mixed mode loading and the meshes at (a) $u = 0.3065 \text{ mm}$, (b) $u = 1.5105 \text{ mm}$.

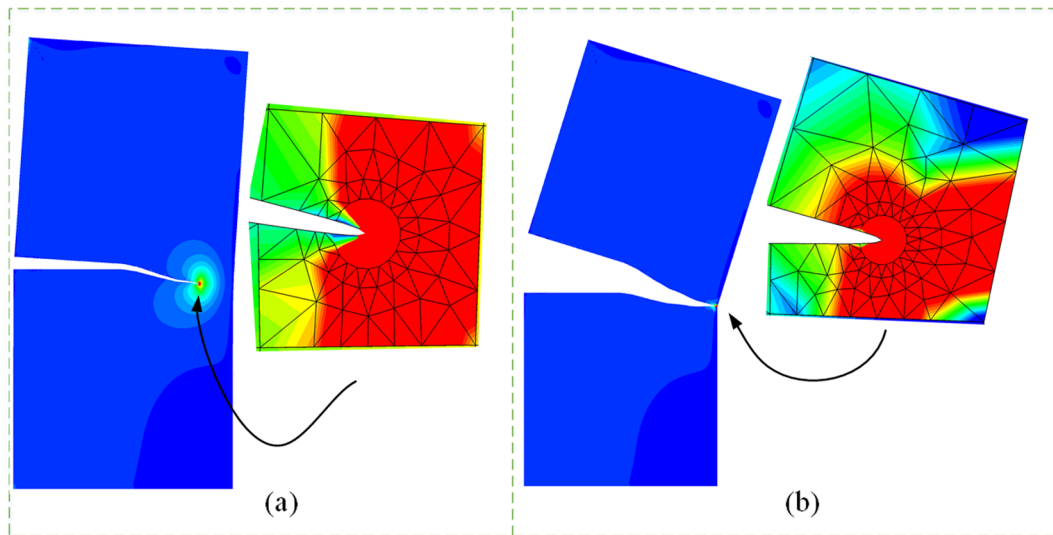


Fig. 15. Contours of first principle stress and the interior mesh of the mixed mode crack at (a) $u = 0.3065$ mm, (b) $u = 1.5105$ mm.

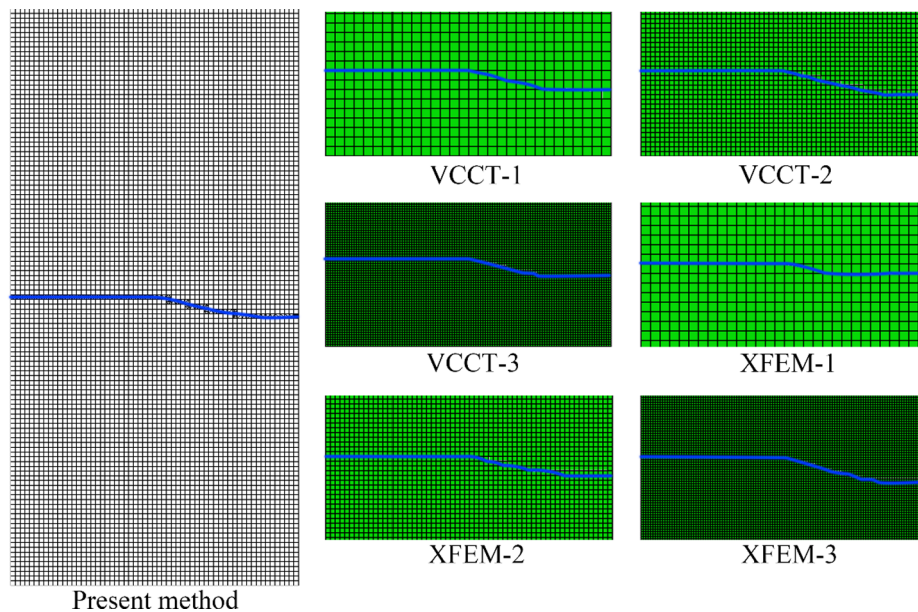


Fig. 16. Predicted crack paths using different methods and meshes. The numbers of elements for different meshes are: present method 7200, VCCT-1 1800, VCCT-2 7200, VCCT-3 28800, XFEM-1 1800, XFEM-2 7200 and XFEM-3 28800.

other, but the present prediction is smoother.

7.2. Edge crack (mixed mode)

Let us consider the edge cracked plate again but with different loading and constraint conditions as depicted in Fig. 14. The material properties are identical with the ones in the numerical example 1. The plate is initially divided into 7200 rectangular elements. The external loading has generated a mixed mode crack and the crack propagation path drifts off from the straight line of the mode I crack path. The meshes at different loading stages are also shown in Fig. 14. The contours of stress as well as the interior mesh of the crack-tip element are shown in Fig. 15. The extreme case, where the crack tip arrives at the last element to the boundary of the plate depicted in Fig. 15(b), can still be modelled, indicating the robustness of the proposed method.

Two other methods i.e., the VCCT and the XFEM from the commercial FE package Abaqus [72] are also employed to study the problem. The Abaqus implementation of XFEM is essentially the PNM with

a cohesive zone model for fracture. The predicted crack paths with different methods and meshes on the un-deformed structure are depicted in Fig. 16. All the predictions are generally in line with each other except XFEM-1 which uses 1800 elements. Nevertheless, the numerical prediction with the XFEM is improved after mesh refinement, i.e., XFEM-2 and XFEM-3. The load–displacement curves with different methods are depicted in Fig. 17. It is found that the results obtained using VCCT with different mesh sizes do not agree with each other. Moreover, significant disagreements are found between the results of VCCT-1 and VCCT-3 and those of other methods. For a fracture process under mixed mode loading condition, those observations indicate that VCCT gives qualitatively correct predictions in terms of crack path but fails in giving quantitatively accurate predictions in terms of the load–displacement response. According to numerical example 1, it is shown that VCCT is more suitable for mode I cracks, and this might be due to the fact that VCCT originally assumes a self-similar crack propagation path. Results obtained with the XFEM in which new segments of a crack are based on cohesive zone model are more reliable. With

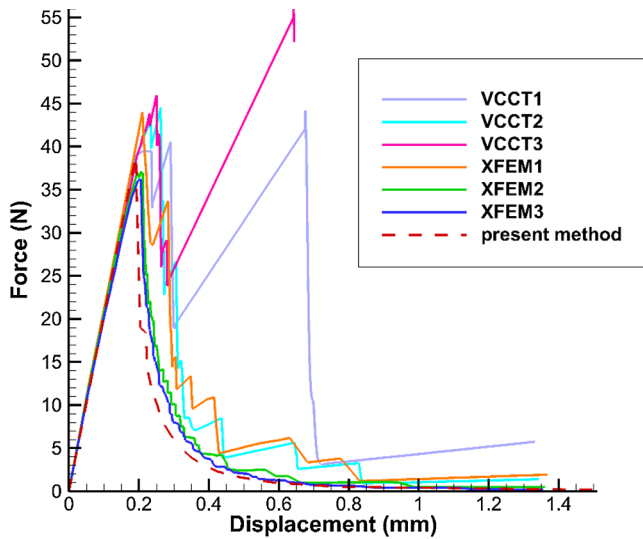


Fig. 17. Load-displacement curves obtained with different methods and meshes. The numbers of elements for different meshes are: present method 7200, VCCT-1 1800, VCCT-2 7200, VCCT-3 28800, XFEM-1 1800, XFEM-2 7200 and XFEM-3 28800.

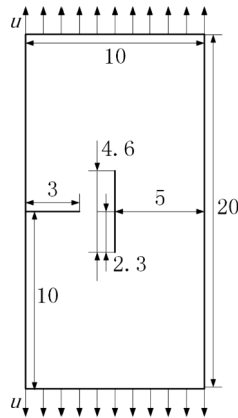


Fig. 18. Geometric information of a plate with two cracks (mm).

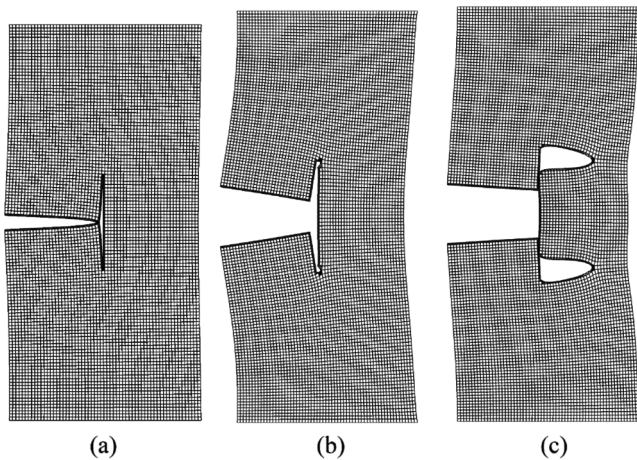


Fig. 19. Mesh at different loading stages, (a) $u = 0.020948814$ mm, (b) $u = 0.095688240$ mm, (c) $u = 0.095688243$ mm.

mesh refinement, the prediction of the load–displacement curve with the XFEM approaches the present prediction. The present results are generally more smooth than all the other results.

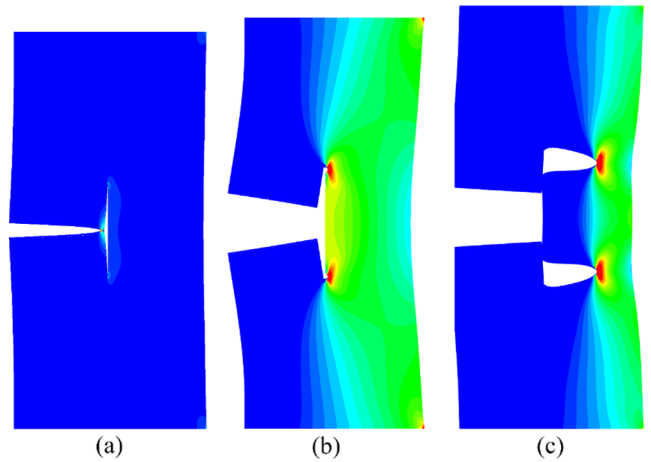


Fig. 20. Plate with two cracks. The first principal stress field at displacements, (a) $u = 0.020948814$ mm, (b) $u = 0.095688240$ mm, (c) $u = 0.095688243$.

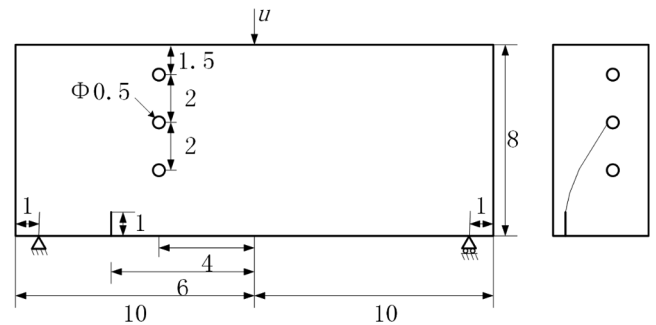


Fig. 21. Cracked panel with three holes. (a) Sketch of specimen, (b) Experimental observation of crack path.

7.3. Plate with two cracks

Now let us consider a plate with two existing cracks as shown in Fig. 18. The material properties are identical with the ones in the numerical example 1. The plate is initially divided into 7381 rectangle elements. The plate is subjected to mode I loading condition and hence the deformation of the structure is symmetric. In the beginning, the left crack which is perpendicular to the loading path starts to grow until it reaches the vertical crack as shown in Fig. 19(a). The two cracks coalesce and the edge crack is arrested. At this instant, the two crack tips of the vertical crack are loaded. Since the vertical crack is parallel to the loading path, the two crack tips are mode II dominated. The predicted crack propagation path of the two crack tips are inclined to the original crack as shown in Fig. 19(b). For any crack tip, the crack propagation angle keeps changing until the propagation path is normal to the loading path as shown in Fig. 19(c). The load increment from Fig. 19(b) to (c) is quite small, indicating the fracture process which happens in an instant is unstable. The fracture process between Fig. 19(b) and (c) forms a blunt corner of the crack trajectory. Upon further increase of the external loading, the crack direction remains unchanged until the plate is fully separated. Contours of the first principle stress at different loading stages are shown in Fig. 20.

7.4. Three point bending (TPB) specimen

A TPB test is investigated in this example. The untested specimen has three holes and a crack in it as shown in Fig. 21. The geometric information as well as the locations of the holes and the crack are also illustrated in Fig. 21. The material properties are: Lamé constants $\lambda = 1.2 \times 10^4 \text{MPa}$, $\mu = 8 \times 10^3 \text{MPa}$ and the fracture energy $G_C = 1 \text{N/mm}$. According to the experimental observations [73], it is

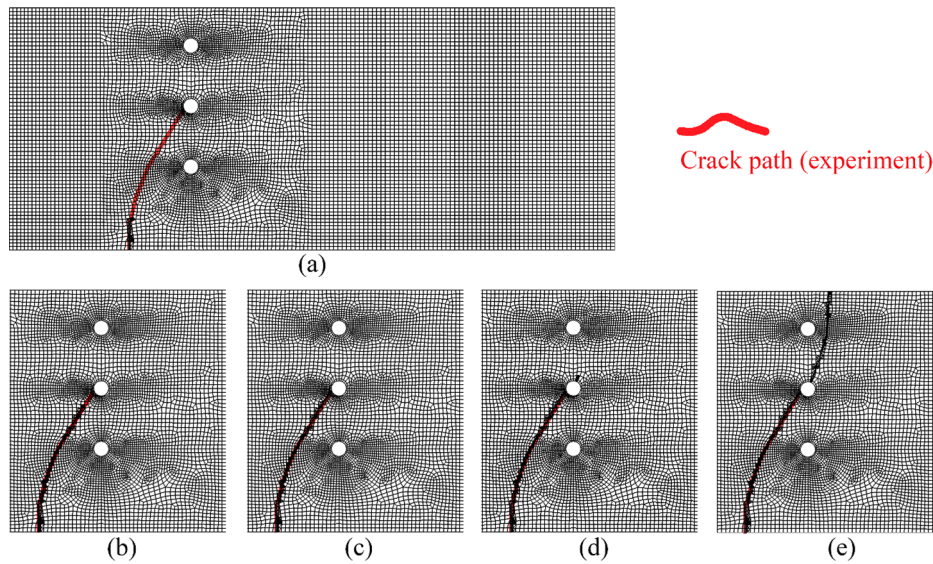


Fig. 22. Crack path at different loading stages, (a) $u = 0.1704$ mm, (b) $u = 0.2162$ mm, (c) $u = 0.2375$ mm, (d) $u = 0.2414$ mm, (e) $u = 0.6950$ mm. Experimental result is referred to [73]

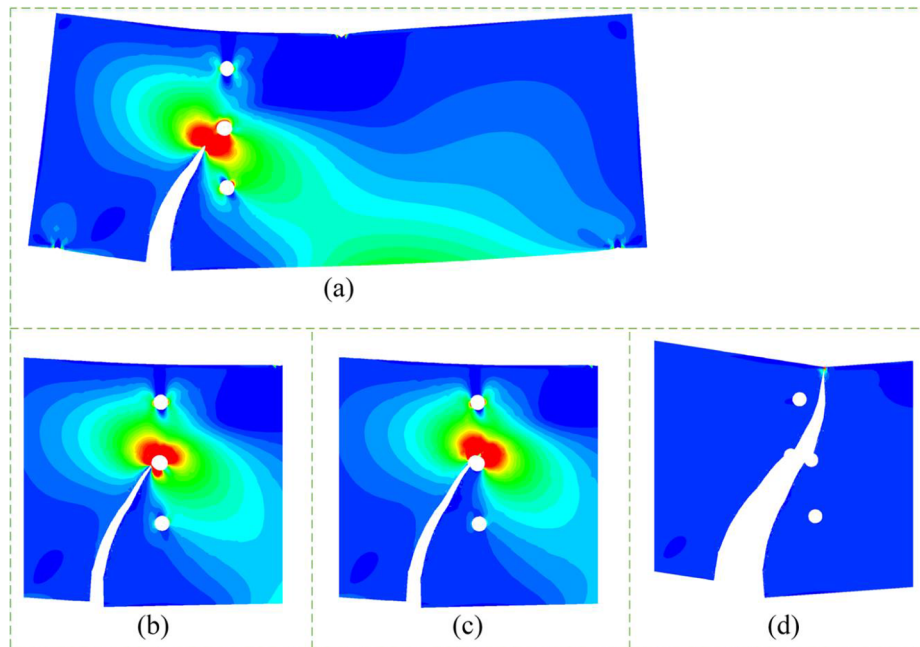


Fig. 23. Contours at different loading stages, (a) $u = 0.2162$ mm, (b) $u = 0.2375$ mm, (c) $u = 0.2414$ mm, (d) $u = 0.6950$ mm.

known that the crack eventually propagates into the middle hole. The crack path observed in the experiment is shown in the right of Fig. 21. During the modelling, the specimen is originally divided into 11,421 elements, rectangular elements cannot be ensured due to the existence of the holes. The crack trajectory at different loading stages are depicted in Fig. 22, in which only the area close to the crack is shown in the sub-figures (b)-(e). It may also be noted that the results in Fig. 22 are given on the un-deformed topology of the plate to better show the crack trajectory. In the early stage, the crack is attracted by the defects (holes) of the plate and is eventually arrested by the middle hole of the plate. The experimental result of the crack path is also marked in the sub-figures, and the modelling results agree excellently with the

experimental observation. Contours of the first principle stress are provided in Fig. 23. When the crack is arrested, the stress concentration in Fig. 23(b) is mainly caused by the hole as the plate is temporarily free from crack tip. A new crack is nucleated with increasing loading when the criterion Eq. (45) is satisfied. The new crack is initiated from the edge of the middle hole as shown in Fig. 22(d) or Fig. 23(c). After that, the new crack keeps growing until the separation of the specimen.

7.5. Compact tension (CT) specimen

A CT specimen is considered in this example. The geometric information as well as the constraint conditions are shown in Fig. 24. A

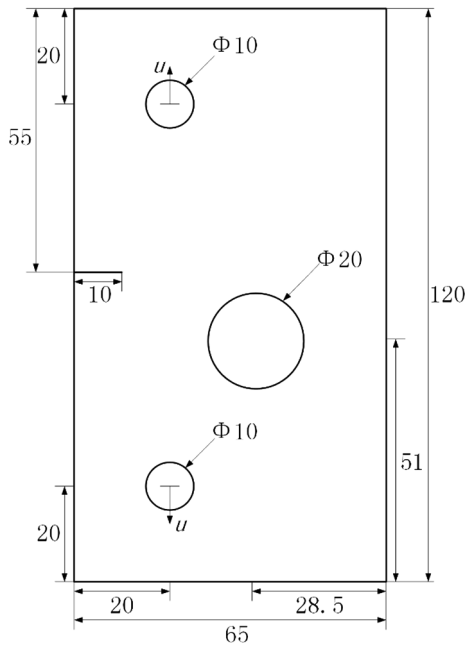


Fig. 24. Cracked panel with a hole. (a) Sketch of specimen.

hole is placed in the center of the plate in prior to the test. The material properties are given as follows: the Lamé constants $\lambda = 1.94 \times 10^3 \text{MPa}$, $\mu = 2.45 \times 10^3 \text{MPa}$ and the fracture energy $G_c = 2.28 \text{N/mm}$. The plate is originally divided into 2886 elements and the elements on the potential crack path are refined to improve the modelling efficiency. Crack patterns are shown in Fig. 25 in which the zone of possible crack paths observed in the experiment [74] is marked in the sub-figures, and the present prediction is in line with the experimental result. When the crack propagates close to the hole, the stress in the area between the crack tip and the hole is raised as depicted Fig. 26. The correlation between the propagating crack and the existing defect has a strong impact on the local response of the fracture process. The crack propagation direction is changed as a result. After the crack enters the hole, the structure is temporarily safe from being cracked until the first principle stress reaching to the critical value.

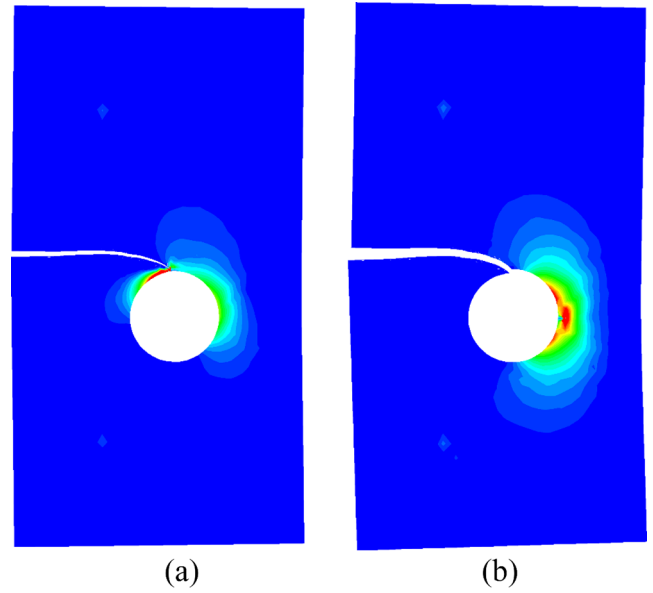


Fig. 26. Contours of the first principle stress at (a) $u = 0.4290 \text{ mm}$, (b) $u = 0.9017 \text{ mm}$.

8. Conclusion

In this contribution, a crack-tip element is proposed for modelling crack propagation. Take the advantages of the symplectic analytical singular element (SASE) and the floating node method (FNM), accurate crack tip fields (displacement and stress) can be captured and multiple crack propagations can be modelled without remeshing. This is essentially because of the use of the crack tip asymptotic analytical solution with higher order expanding terms. Another benefit of the proposed method is that the stress intensity factors (SIFs) can be solved without any post-processing. In comparison with other methods which use domain integral for the calculation of SIFs, the proposed method is not limited in dealing with the extreme case where the crack tip is propagating close to the boundary of a structure. The results of the present work have demonstrated the potential of the proposed SASE-FNM method for the accurate and robust modelling of arbitrary crack propagation problems in structures of complex geometries.

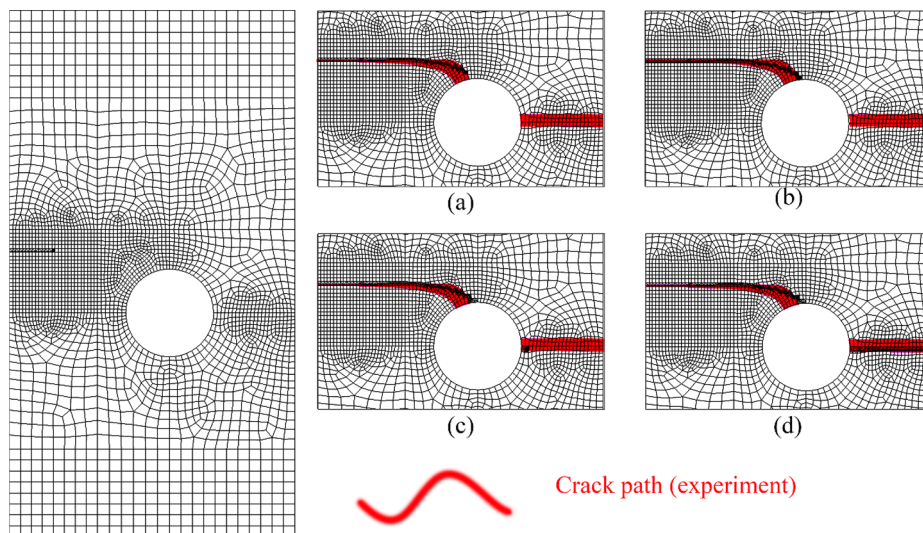


Fig. 25. Deformation of the specimen at different loading stages, (a) $u = 0.3723 \text{ mm}$, (b) $u = 0.4290 \text{ mm}$, (c) $u = 0.9107 \text{ mm}$, (d) $u = 5.5707 \text{ mm}$. Experimental result is referred to [74].

Acknowledgement

This work was supported by the National Natural Science Foundation of China (No. 11872143), the Fundamental Research Funds for the Central Universities (DUT18LK06) and the National Key Research and Development Program of China [No. 2016YFB0200702].

References

- [1] N. Moës, J. Dolbow, T. Belytschko, A finite element method for crack growth without remeshing, *Int. J. Num. Meth. Eng.* 46 (1999) 131–150.
- [2] L.F. Kawashita, A. Bedos, S.R. Hallett, Modelling mesh independent transverse cracks in laminated composites with a simplified cohesive segment method, *Comput. Mater. Cont.* 32 (2012) 133–158.
- [3] J.Y. Wu, F.B. Li, An improved stable XFEM (Is-XFEM) with a novel enrichment function for the computational modeling of cohesive cracks, *Comput. Methods Appl. Mech. Eng.* 295 (2015) 77–107.
- [4] S. Bhattacharya, I.V. Singh, B.K. Mishra, T.Q. Bui, Fatigue crack growth simulations of interfacial cracks in bi-layered FGMs using XFEM, *Comput. Mech.* 52 (2013) 799–814.
- [5] Z. Wang, T. Yu, T.Q. Bui, N.A. Trinh, N.T.H. Luong, N.D. Duc, D.H. Doan, Numerical modeling of 3-D inclusions and voids by a novel adaptive XFEM, *Adv. Eng. Softw.* 102 (2016) 105–122.
- [6] T. Nagashima, H. Suemasu, X-FEM analyses of a thin-walled composite shell structure with a delamination, *Compos. Struct.* 88 (2010) 549–557.
- [7] T. Hettich, A. Hund, E. Ramm, Modeling of failure in composites by X-FEM and level sets within a multiscale framework, *Comput. Methods Appl. Mech. Eng.* 197 (2008) 414–424.
- [8] X.F. Hu, B.Y. Chen, M. Tirvaudey, V.B.C. Tan, T.E. Tay, Integrated XFEM-CE analysis of delamination migration in multi-directional composite laminates, *Compos. A Appl. Sci. Manuf.* 90 (2016) 161–173.
- [9] S. Kumar, I.V. Singh, B.K. Mishra, T. Rabczuk, Modeling and simulation of kinked cracks by virtual node XFEM, *Comput. Methods Appl. Mech. Eng.* 283 (2015) 1425–1466.
- [10] S. Kumar, I.V. Singh, B.K. Mishra, K. Sharma, I.A. Khan, A homogenized multigrid XFEM to predict the crack growth behavior of ductile material in the presence of microstructural defects, *Eng. Fract. Mech.* (2016).
- [11] P.M.A. Areias, T. Belytschko, A comment on the article “A finite element method for simulation of strong and weak discontinuities in solid mechanics” By A. Hansbo, P. Hansbo [Comp. Meth. Appl. Mech. Engrg. 193 (2004) 3523–3540], *Comput. Methods Appl. Mech. Eng.* 195 (2006) 1275–1276.
- [12] N. Sukumar, Z.Y. Huang, J.H. Prevost, Z. Suo, Partition of unity enrichment for bimaterial interface cracks, *Int. J. Num. Meth. Eng.* 59 (2004) 1075–1102.
- [13] A. Hansbo, P. Hansbo, A finite element method for the simulation of strong and weak discontinuities in solid mechanics, *Comput. Methods Appl. Mech. Eng.* 193 (2004) 3523–3540.
- [14] P.M.A. Areias, J.H. Song, T. Belytschko, Analysis of fracture in thin shells by overlapping paired elements, *Comput. Methods Appl. Mech. Eng.* 195 (2006) 5343–5360.
- [15] J.H. Song, P.M.A. Areias, T. Belytschko, A method for dynamic crack and shear band propagation with phantom nodes, *Int. J. Num. Meth. Eng.* 67 (2006) 868–893.
- [16] J. Mergheim, E. Kuhl, P. Steinmann, A finite element method for the computational modelling of cohesive cracks, *Int. J. Num. Meth. Eng.* 63 (2005) 276–289.
- [17] T. Rabczuk, G. Zi, A. Gerstenberger, W.A. Wall, A new crack-tip element for the phantom-node method with arbitrary cohesive cracks, *Int. J. Num. Meth. Eng.* 75 (2008) 577–599.
- [18] X.J. Fang, Q.D. Yang, B.N. Cox, Z.Q. Zhou, An augmented cohesive zone element for arbitrary crack coalescence and bifurcation in heterogeneous materials, *Int. J. Num. Meth. Eng.* 88 (2011) 841–861.
- [19] J. Mergheim, E. Kuhl, P. Steinmann, Towards the algorithmic treatment of 3D strong discontinuities, *Commun. Numer. Methods Eng.* 23 (2007) 97–108.
- [20] D.S. Ling, Q.D. Yang, B. Cox, An augmented finite element method for modeling arbitrary discontinuities in composite materials, *Int. J. Fract.* 156 (2009) 53–73.
- [21] F.P. van der Meer, L.J. Sluys, A phantom node formulation with mixed mode cohesive law for splitting in laminates, *Int. J. Fract.* 158 (2009) 107–124.
- [22] X.J. Fang, Z.Q. Zhou, B.N. Cox, Q.D. Yang, High-fidelity simulations of multiple fracture processes in a laminated composite in tension, *J. Mech. Phys. Solids* 59 (2011) 1355–1373.
- [23] N. Sukumar, N. Moes, B. Moran, T. Belytschko, Extended finite element method for three-dimensional crack modelling, *Int. J. Num. Meth. Eng.* 48 (2000) 1549–1570.
- [24] Q. Duan, J.H. Song, T. Menouillard, T. Belytschko, Element-local level set method for three-dimensional dynamic crack growth, *Int. J. Num. Meth. Eng.* 80 (2009) 1520–1543.
- [25] J. Mergheim, A variational multiscale method to model crack propagation at finite strains, *Int. J. Num. Meth. Eng.* 80 (2009) 269–289.
- [26] C.L. Richardson, J. Hegemann, E. Sifakis, J. Hellrung, J.M. Teran, An XFEM method for modeling geometrically elaborate crack propagation in brittle materials, *Int. J. Num. Meth. Eng.* 88 (2011) 1042–1065.
- [27] T. Chau-Dinh, G. Zi, P.S. Lee, T. Rabczuk, J.H. Song, Phantom-node method for shell models with arbitrary cracks, *Compos. Struct.* 92–93 (2012) 242–256.
- [28] B.Y. Chen, S.T. Pinho, N.V. De Carvalho, P.M. Baiz, T.E. Tay, A floating node method for the modelling of discontinuities in composites, *Eng. Fract. Mech.* 127 (2014) 104–134.
- [29] N.V. De Carvalho, B.Y. Chen, S.T. Pinho, J.G. Ratcliffe, P.M. Baiz, T.E. Tay, Modeling delamination migration in cross-ply tape laminates, *Compos. A Appl. Sci. Manuf.* 71 (2015) 192–203.
- [30] B.Y. Chen, T.E. Tay, S.T. Pinho, V.B.C. Tan, Modelling the tensile failure of composites with the floating node method, *Comput. Methods Appl. Mech. Eng.* 308 (2016) 414–442.
- [31] B.Y. Chen, T.E. Tay, S.T. Pinho, V.B.C. Tan, Modelling delamination migration in angle-ply laminates, *Compos. Sci. Technol.* 142 (2017) 145–155.
- [32] X. Lu, B.Y. Chen, V.B.C. Tan, T.E. Tay, Adaptive floating node method for modelling cohesive fracture of composite materials, *Eng. Fract. Mech.* 194 (2018) 240–261.
- [33] X. Lu, B.Y. Chen, V.B.C. Tan, T.E. Tay, A separable cohesive element for modelling coupled failure in laminated composite materials, *Compos. A Appl. Sci. Manuf.* 107 (2018) 387–398.
- [34] N. Moes, A. Gravouil, T. Belytschko, Non-planar 3D crack growth by the extended finite element and level sets – part I: mechanical model, *Int. J. Num. Meth. Eng.* 53 (2002) 2549–2568.
- [35] X.F. Hu, X. Lu, T.E. Tay, Modelling delamination migration using virtual embedded cohesive elements formed through floating nodes, *Compos. Struct.* 204 (2018) 500–512.
- [36] M. McElroy, Use of an enriched shell finite element to simulate delamination-migration in a composite laminate, *Compos. Struct.* 167 (2017) 88–95.
- [37] J. Zhi, T.E. Tay, Explicit modelling of matrix cracking and delamination in laminated composites with discontinuous solid-shell elements, *Comput. Methods Appl. Mech. Eng.* 351 (2019) 60–84.
- [38] S. Kumar, Y. Wang, L.H. Poh, B.Y. Chen, Floating node method with domain-based interaction integral for generic 2D crack growths, *Theor. Appl. Fract. Mech.* 96 (2018) 483–496.
- [39] J. Zhi, B.Y. Chen, T.E. Tay, Geometrically nonlinear analysis of matrix cracking and delamination in composites with floating node method, *Comput. Mech.* 63 (2019) 201–217.
- [40] E.S. Kocaman, B.Y. Chen, S.T. Pinho, A polymorphic element formulation towards multiscale modelling of composite structures, *Comput. Methods Appl. Mech. Eng.* 346 (2019) 359–387.
- [41] R.S. Barsoum, Triangular quarter-point elements as elastic and perfectly-plastic crack tip elements, *Int. J. Num. Meth. Eng.* 11 (1977) 85–98.
- [42] S.E. Benzley, Representation of singularities with isoparametric finite elements, *Int. J. Num. Meth. Eng.* 8 (1974) 537–545.
- [43] T. Menouillard, J.H. Song, Q.L. Duan, T. Belytschko, Time dependent crack tip enrichment for dynamic crack propagation, *Int. J. Fract.* 162 (2010) 33–49.
- [44] H. Bayesteh, S. Mohammadi, XFEM fracture analysis of shells: the effect of crack tip enrichments, *Comput. Mater. Sci.* 50 (2011) 2793–2813.
- [45] A. Gravouil, N. Moes, T. Belytschko, Non-planar 3D crack growth by the extended finite element and level sets – part II: level set update, *Int. J. Num. Meth. Eng.* 53 (2002) 2569–2586.
- [46] L. Bouhala, Q. Shao, Y. Koutsawa, A. Younes, P. Nunez, A. Makradi, S. Belouettar, An XFEM crack-tip enrichment for a crack terminating at a bi-material interface, *Eng. Fract. Mech.* 102 (2013) 51–64.
- [47] C. Song, J.P. Wolf, The scaled boundary finite-element method—alias consistent infinitesimal finite-element cell method-for elastodynamics, *Comput. Methods Appl. Mech. Eng.* 147 (1997) 329–355.
- [48] J.P. Wolf, *The scaled boundary finite element method*, John Wiley & Sons, 2003.
- [49] S. Kumar, I.V. Singh, B.K. Mishra, A. Singh, New enrichments in XFEM to model dynamic crack response of 2-D elastic solids, *Int. J. Impact Eng.* 87 (2016) 198–211.
- [50] S. Kumar, G. Bhardwaj, A new enrichment scheme in XFEM to model crack growth behavior in ductile materials, *Theor. Appl. Fract. Mech.* 96 (2018) 296–307.
- [51] Q.Z. Xiao, B.L. Karihaloo, Improving the accuracy of XFEM crack tip fields using higher order quadrature and statically admissible stress recovery, *Int. J. Numer. Meth. Eng.* 66 (2006) 1378–1410.
- [52] X.Y. Liu, Q.Z. Xiao, B.L. Karihaloo, XFEM for direct evaluation of mixed mode SIFs in homogeneous and bi-materials, *Int. J. Numer. Meth. Eng.* 59 (2004) 1103–1118.
- [53] K.W. Cheng, T.P. Fries, Higher-order XFEM for curved strong and weak discontinuities, *Int. J. Numer. Meth. Eng.* 82 (2010) 564–590.
- [54] P. Laborde, J. Pommier, Y. Renard, M. Salaun, High-order extended finite element method for cracked domains, *Int. J. Numer. Meth. Eng.* 64 (2005) 354–381.
- [55] J. Bulling, H. Gravenkamp, C. Birk, A high-order finite element technique with automatic treatment of stress singularities by semi-analytical enrichment, *Comput. Methods Appl. Mech. Eng.* 355 (2019) 135–156.
- [56] S. Bordas, T. Rabczuk, G. Zi, Three-dimensional crack initiation, propagation, branching and junction in non-linear materials by an extended meshfree method without asymptotic enrichment, *Eng. Fract. Mech.* 75 (2008) 943–960.
- [57] W.A. Yao, X.F. Hu, A novel singular finite element of mixed-mode crack problems with arbitrary crack tractions, *Mech. Res. Commun.* 38 (2011) 170–175.
- [58] X.F. Hu, W.A. Yao, A new enriched finite element for fatigue crack growth, *Int. J. Fatigue* 48 (2013) 247–256.
- [59] X.F. Hu, T.Q. Bui, J.N. Wang, W.A. Yao, L.H.T. Ton, I.V. Singh, A new cohesive crack tip symplectic analytical singular element involving plastic zone length for fatigue crack growth prediction under variable amplitude cyclic loading, *Eur. J. Mech. A. Solids* 65 (2017) 79–90.
- [60] X.F. Hu, Q.S. Shen, J.N. Wang, W.A. Yao, S.T. Yang, A novel size independent symplectic analytical singular element for inclined crack terminating at bimaterial interface, *Appl. Math. Model.* 50 (2017) 361–379.
- [61] X.F. Hu, W.A. Yao, J.N. Wang, A size independent enriched finite element for the modeling of bimaterial interface cracks, *Comput. Struct.* 172 (2016) 1–10.
- [62] W.A. Yao, X. Li, X.F. Hu, Viscoelastic crack analysis using symplectic analytical singular element combining with precise time-domain algorithm, *Int. J. Fract.* 214 (2018) 29–48.

- [63] X.F. Hu, W.A. Yao, S.T. Yang, A symplectic analytical singular element for steady-state thermal conduction with singularities in anisotropic material, *ASME-J. Heat Transf.* 140 (2018) 091301.
- [64] X.F. Hu, H.Y. Gao, W.A. Yao, S.T. Yang, Study on steady-state thermal conduction with singularities in multi-material composites, *Int. J. Heat Mass Transf.* 104 (2017) 861–870.
- [65] Z.Y. Cai, X.F. Hu, W.A. Yao, Numerical study on bi-material interface crack using symplectic analytical singular element, *Eng. Fract. Mech.* 199 (2018) 308–326.
- [66] W.A. Yao, P. Zhang, H.Y. Gao, X.F. Hu, An analytical singular element for the study of cohesive zone model based crack propagation, *Int. J. Fract.* 197 (2016) 189–199.
- [67] T. Rabczuk, S. Bordas, G. Zi, On three-dimensional modelling of crack growth using partition of unity methods, *Compos. Struct.* 88 (2010) 1391–1411.
- [68] W.A. Yao, W.X. Zhong, C.W. Lim, *Symplectic Elasticity*, World Scientific, 2009.
- [69] Engwirda D, Locally-optimal Delaunay-refinement and optimisation-based mesh generation, Ph.D. Thesis, School of Mathematics and Statistics, The University of Sydney, <https://github.com/dengwirda/mesh2d>.
- [70] Simulia DCS. *Abaqus 6.11 analysis user's manual*. 2011.
- [71] T.N. Bittencourt, P.A. Wawrzynek, A.R. Ingraffea, J.L. Sousa, Quasi-automatic simulation of crack propagation for 2D LEFM problems, *Eng. Fract. Mech.* 55 (1996) 321–334.
- [72] E. Giner, N. Sukumar, J.E. Tarancón, F.J. Fuenmayor, An Abaqus implementation of the extended finite element method, *Eng. Fract. Mech.* 76 (2009) 347–368.
- [73] J. Shi, D. Chopp, J. Lua, N. Sukumar, T. Belytschko, Abaqus implementation of extended finite element method using a level set representation for three-dimensional fatigue crack growth and life predictions, *Eng. Fract. Mech.* 77 (2010) 2840–2863.
- [74] J.J.C. Remmers, R. de Borst, A. Needleman, A cohesive segments method for the simulation of crack growth, *Comput. Mech.* 31 (2003) 69–77.